# SUPPORTING MATERIAL

## FOR

## Mechanism of size-dependent segregation at the immune synapse determined with molecular rulers

Juha-Matti Alakoskela, Apurba L. Koner, Dominika Rudnicka, Karsten Köhler, Mark Howarth, Daniel M. Davis*

## MATERIALS AND METHODS

### *Image analysis*

To estimate the level of spatial correlation between the fluorescence intensities of GFP-tagged proteins and the fluorescent size series, several optical (Z-) slices of each synapse were analyzed in MATLAB (MathWorks, Natick, MA, USA). An outline of a cell membrane was expanded along the direction of the selection (i.e. membrane) normal, until the pixels showing membrane intensities were within the selected region (see Fig. S1 *A* in Supporting Material). The intensities in each fluorescence channel for the pixels in the direction of the normal (≈membrane normal) were integrated to obtain the integrated intensity in each channel as a function of position along membrane perimeter. Since both cell types were labeled with different membrane-associated labels in all experiments, we could estimate the cell–cell contact, i.e. the limits of synapse, by determining where the different membrane stains overlapped (see Fig. S1 *B*). Fluorescence intensities in different channels at the synapse were plotted against each other and Pearson correlation coefficients calculated. This procedure was repeated for several slices throughout a given cell-cell conjugate and the average correlation coefficient for a given synapse was calculated.

Areas and relative concentrations of the fluorophores in the central and peripheral zone of the cell–cell contact were determined as follows: First, points from the center line of the membrane were picked manually from different z slices through the cell-cell conjugate. Then values were converted to the cylindrical coordinate system, and the cubic interpolation function of MATLAB was used to interpolate the radius from cell center to membrane center for each angle across each z slice. For the intensity along the membrane, the fluorescence intensity was integrated in the direction of local membrane normal across four pixels on either side of the membrane center line. Both 3D reconstructions of the data as well as 2D projections were created (see Fig. S1 *C*). Any projection of a spherical surface in 2D requires compromises (as in maps of Earth, for instance). To facilitate intensity and area calculations, we chose projections that maintain the area and hence the total intensity of the surface although this leads to distortion in the 2D projection of the shapes on the 3D surface. For the analysis of intensities and areas, the outline of the cell–cell contact was drawn into the 2D projection based on the membrane stains overlapping between the two cells, and regions that had high HLA-Cw6-GFP intensity were marked (see Fig. S1 *D*).

To estimate the surface density of receptors, in some cases 3D reconstructions were created semi-automatically with the aid of the 3D version of a region scalable segmentation algorithm (S2). First, as pre-processing for the 3D segmentation, image stacks were smoothed by a smoothing algorithm (S3). After this, a local minimum in a 5×5×5 neighborhood of the resulting stack was smoothed by Gaussian kernel (kernel width = 15 pixels, $\sigma$ = 2.5 pixels) and subtracted, setting negative values to zero. Then the stack was reduced in size by factor of 4 in xy directions and factor of 2 in z direction. A 3D version of the hybrid model filtering (S4) was used for smoothing the rescaled stack. Finally, the intensity was normalized in a 5×5×5 local neighborhood, setting the value within each pixel to be

$$I_{NEW} = (I_{OLD}-I_{MIN})/(0.2\times S_{MAX}+0.8\times I_{MAX}-I_{MIN})$$

where $I_{OLD}$ is the original intensity of the pixel, $I_{MIN}$ is the minimum intensity of local neighborhood, $S_{MAX}$ is the maximum of the intensity scale (255 for 8-bit image), and $I_{MAX}$ is the maximum intensity of local neighborhood. The $S_{MAX}$ term suppresses high values from low intensity noise in empty regions in the stack. This normalization causes some problems in large regions of nearly equal intensity, but enhances visibility of edges (see Fig. S2 for the effects of various steps in pre-processing).

The segmentation algorithm was then run on this stack to find the external and internal borders of plasma membrane, and the results were corrected manually in MATLAB. In most cases the segmentation results at the very bottom and at the top of the cell required manual modification, i.e. joining the holes left partly resulting from the normalization procedure, likewise the intracellular clusters of fluorescence in the immediate vicinity of the plasma membrane and the other cells in contact needed to be manually separated from the plasma membrane (see Fig. S3 for a comparison of automated and manually modified results). After satisfactory segmentation, the volume of the cell, plasma membrane, and intracellular components were calculated based on the total volume of voxels in these compartments. The total (as well as mean and median) intensities in different channels for each compartment were calculated from the intensities of voxels within each compartment. It is important to note that the final, manual correction of the compartment borders as well as all the calculations were done using the original, unmodified image data. The surface triangularization of the isosurface of the image energy matrix produced by the algorithm and manual corrections was computed in MATLAB. The external membrane area was calculated based on the total area of triangles in the surface triangularization. Based on the data from this analysis and the surface expression level of HLA-Cw6 from the flow cytometry analysis the surface densities of HLA-Cw6-GFP within the peripheral zone of the synapse were calculated (see Table S1 in Supporting Material).

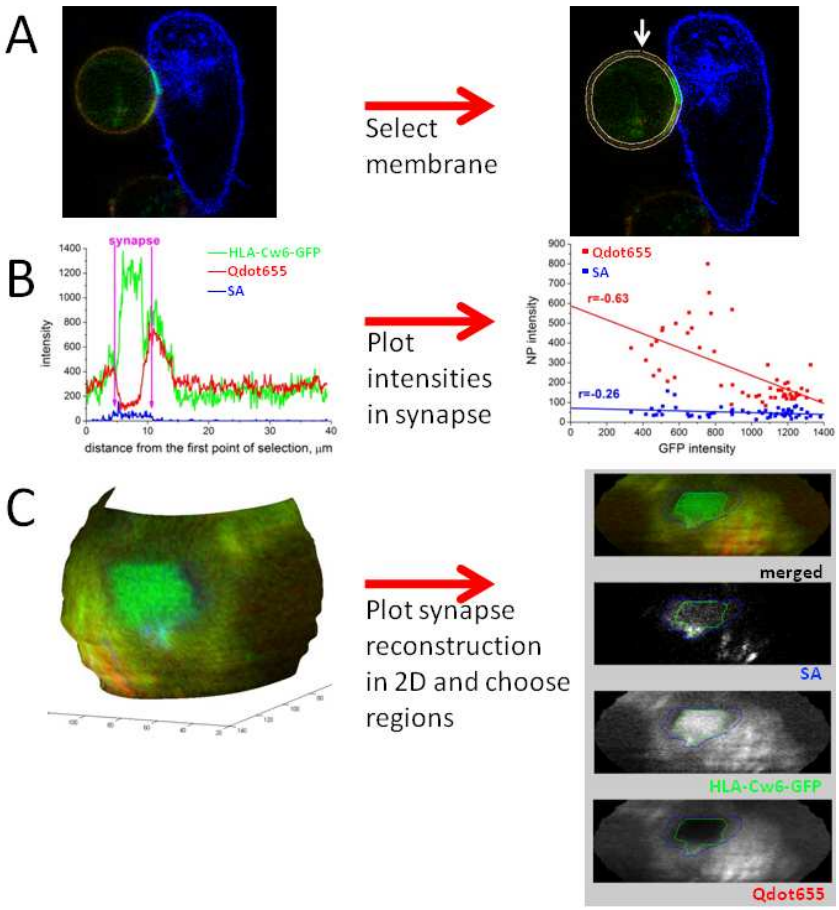


**Figure S1**. The analysis process. In *(A)* the selection of membrane is shown; the blue channel intensities were rescaled to enhance visibility. The intensities across the membrane in the direction of selection normal are then integrated and plotted against the distance along the selection (arrow shows the beginning of selection). *(B)* Left, the intensities plotted against the distance along the selection. Colors correspond to one in merged images in *(A)*. The intensity of the stain in the membrane of the other cell (blue line in *(B)* on the left) is then used to define the limits of the synapse (magenta arrows), and the correlations for the intensities against the GFP intensity are then calculated from the line fits (*(B)*, right). For the analysis of intensity distributions in the central and peripheral zone of the synapse a 3D reconstruction of the synapse was spread into two dimensions *(C)*, and the outer perimeter of the synapse was outlined based on the overlap with the stain in the other cell (thin blue line in *(C)*, right) and the central zone was chosen based on where GFP fluorescence was particularly intense in the mature, i.e. late-stage, synapse (thin green line in *(C)*, right).

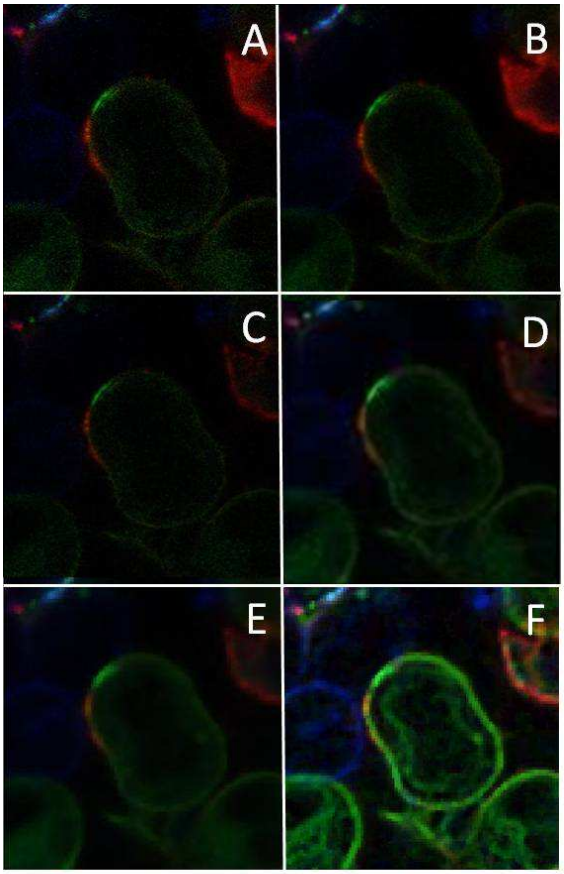


**Figure S2.** Image preprocessing steps for the semi-automated cell perimeter finding (see section *Image Analysis* for details). In *(A)* unmodified image is shown, in *(B)* image smoothed by Garcia algorithm, in *(C)* an image with local background subtraction, in *(D)* the image from the stack reduced in size by 4-fold in x and y directions and 2-fold in z direction, in *(E)* the 3D hybrid model-smoothed image, and in *(F)* the image with local normalization.

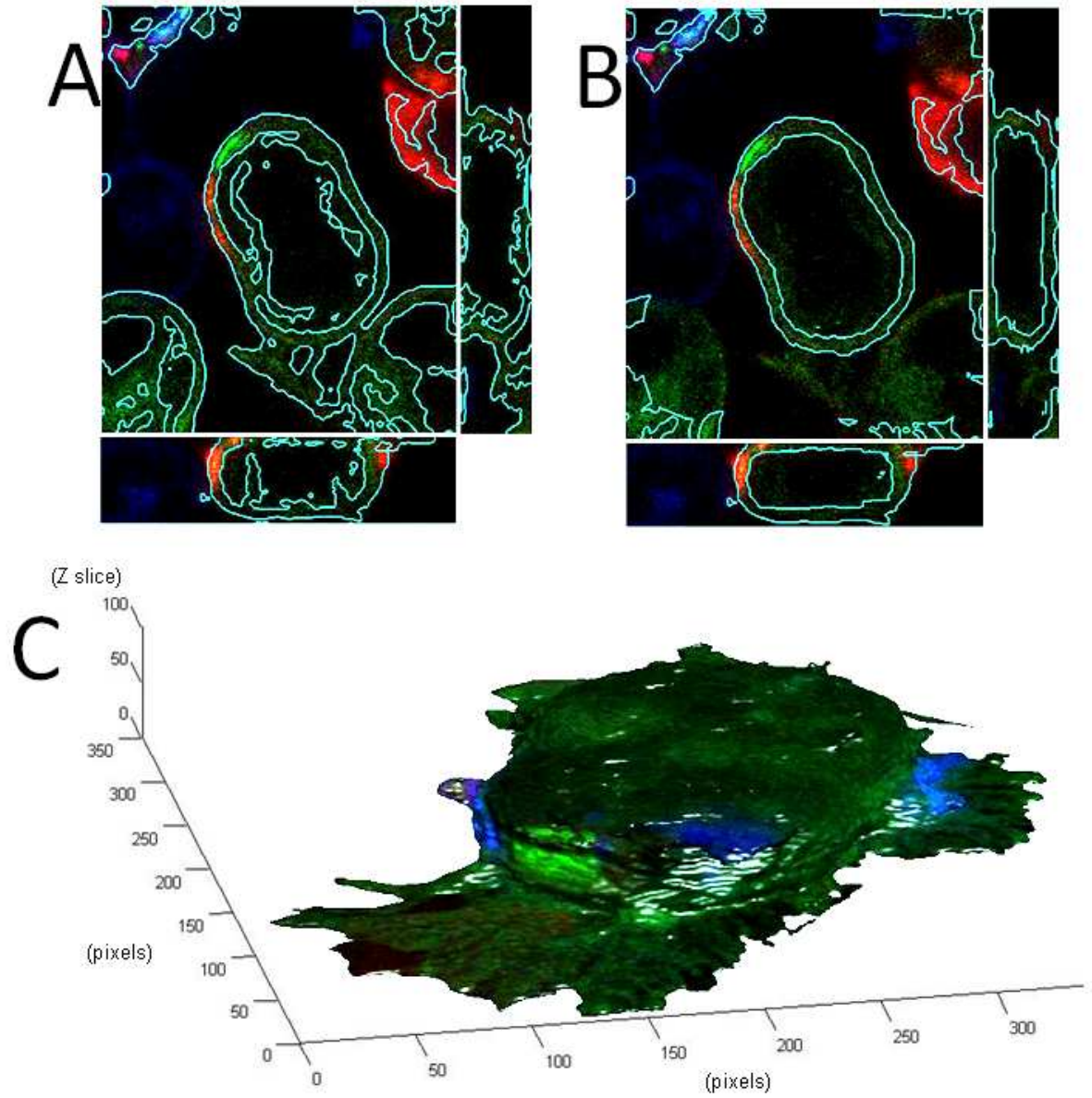


**Figure S3.** Example of an automatic border finding result and a manually corrected result. In *(A)* the result of the segmentation method operating on the pre-processed stack (see Fig. S2 *F*) is shown. This image shows all the common problems, partly resulting from pre-processing (though it avoids other problems): the cell is connected to nearby cells, and the bottom and top of the cell have many holes. In *(B)* the manually corrected result is shown. This result can then be used to pick from the stack automatically all the closed volumes and the subvolumes within these volumes and analyze their intensities. In *(C)* a view of the resulting 3D representation of the cell surface is shown.

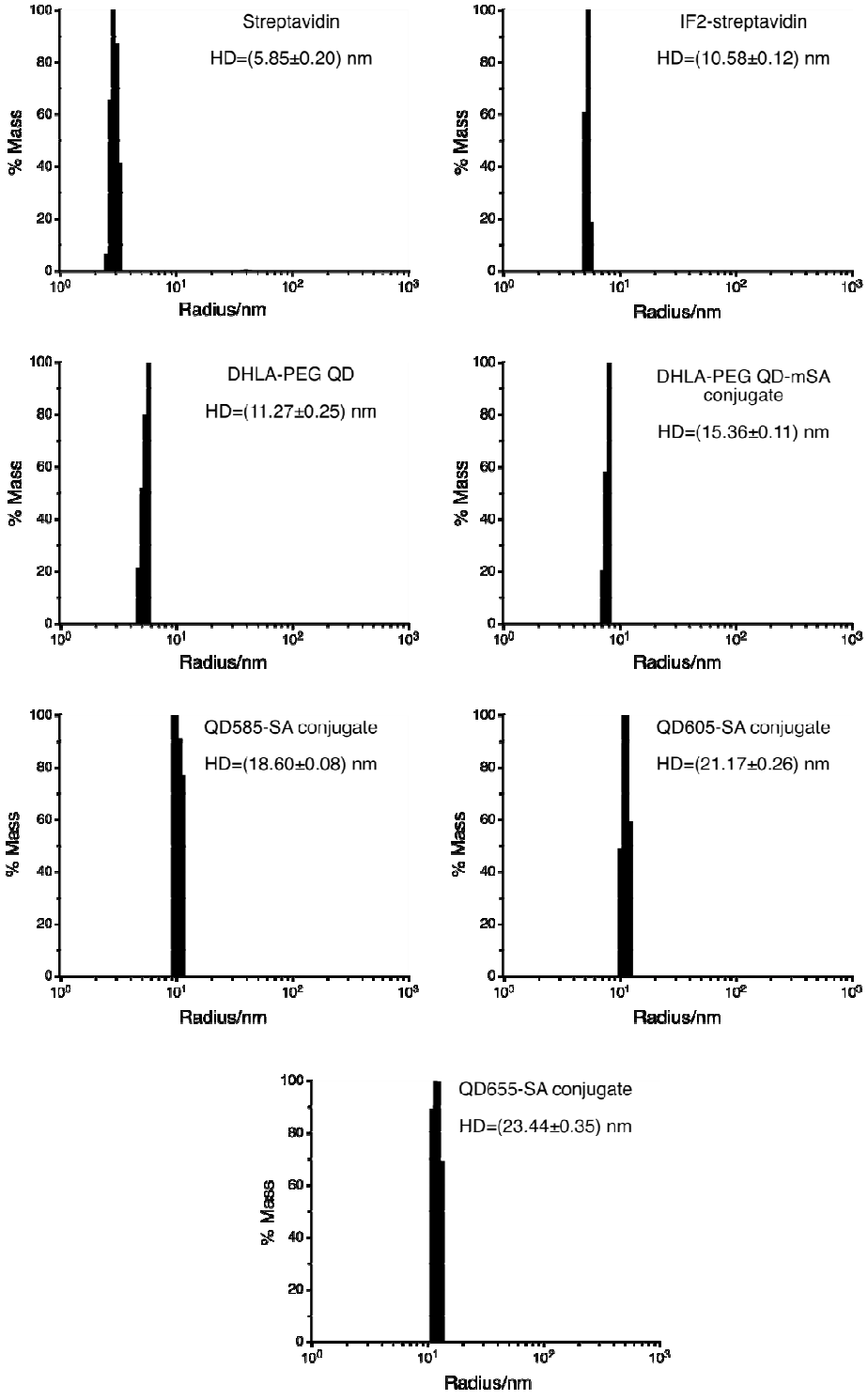


**Figure S4.** Hydrodynamic size determination using dynamic light scattering. Hydrodynamic diameters (HD) from triplicate measurements ± 1 s.d. are shown for streptavidin, IF2-streptavidin, DHLA-PEG quantum dots (QDs), DHLA-PEG QDs conjugated with monovalent streptavidin, QD585-SA conjugate, QD605-SA conjugate, and QD655-SA conjugate.

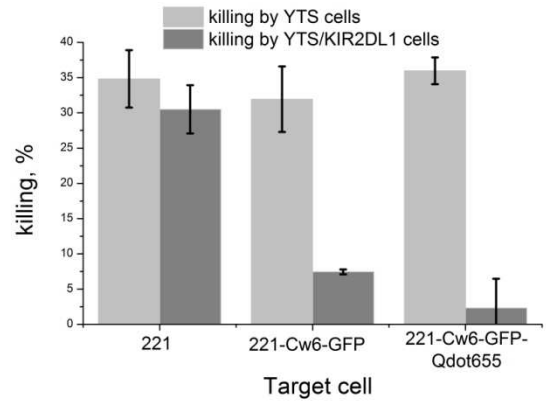


**Figure S5.** Assay for NK cell function in the presence of nanoparticle Qdot655. The light gray columns indicate killing by YTS cells and the dark gray columns the killing by YTS/KIR2DL1 for the indicated three target cells: normal 221, 221/Cw6-GFP, and 221/Cw6-GFP labeled with 23.4 nm Qdot655. The error bars indicate standard deviation of three samples. Note that the recognition of class I MCH molecule (Cw6-GFP) by the inhibitory NK cell receptor KIR2DL1 (dark gray) on YTS cells leads to decreased killing of the 221 cells, both in unlabeled and labeled cells, whereas no significant decrease in killing is seen for YTS cells not expressing KIR2DL1 (light gray).

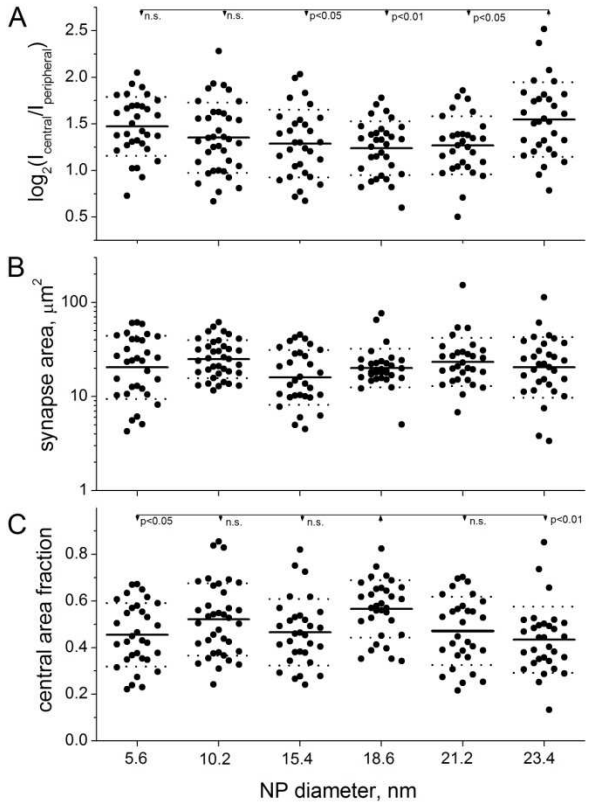


**Figure S6**. The synapse characteristics in the presence of different-sized fluorescent particles on 221/Cw6-GFP cells. In *(A)* the base two logarithm of Cw6-GFP central/peripheral intensity ratio is shown. The central/peripheral intensity ratio of Cw6-GFP showed minor but statistically significant differences (ANOVA p=0.002) for different fluorescent particles, with post hoc tests revealing that the Cw6-GFP intensity ratio for 23.4 nm particles was significantly different from that for 18.6 nm particles ($p<0.01$) and those for 15.4 and 21.2

nm particles ($p<0.05$) while other differences were not statistically significant. These differences may be either coincidental, or alternatively, the largest particles that are not efficiently excluded from the synapse (i.e. 18.6 nm and 15.4 nm particles) may be the most efficient in excluding Cw6-GFP from the synapse. In *(B)* the areas of the synapses are shown. The synapse area was not significantly different with different fluorescent particles (ANOVA: $p = 0.085$). In *(C)* the fractions of the central area/total synapse area are shown. The fraction of central area (ANOVA $p=0.002$) of the total area had a small but statistically significant difference when comparing 18.6 nm particles to 5.9 nm ($p<0.05$) or 23.4 nm (43.4 %, $p<0.01$) particles – other differences were not statistically significant.

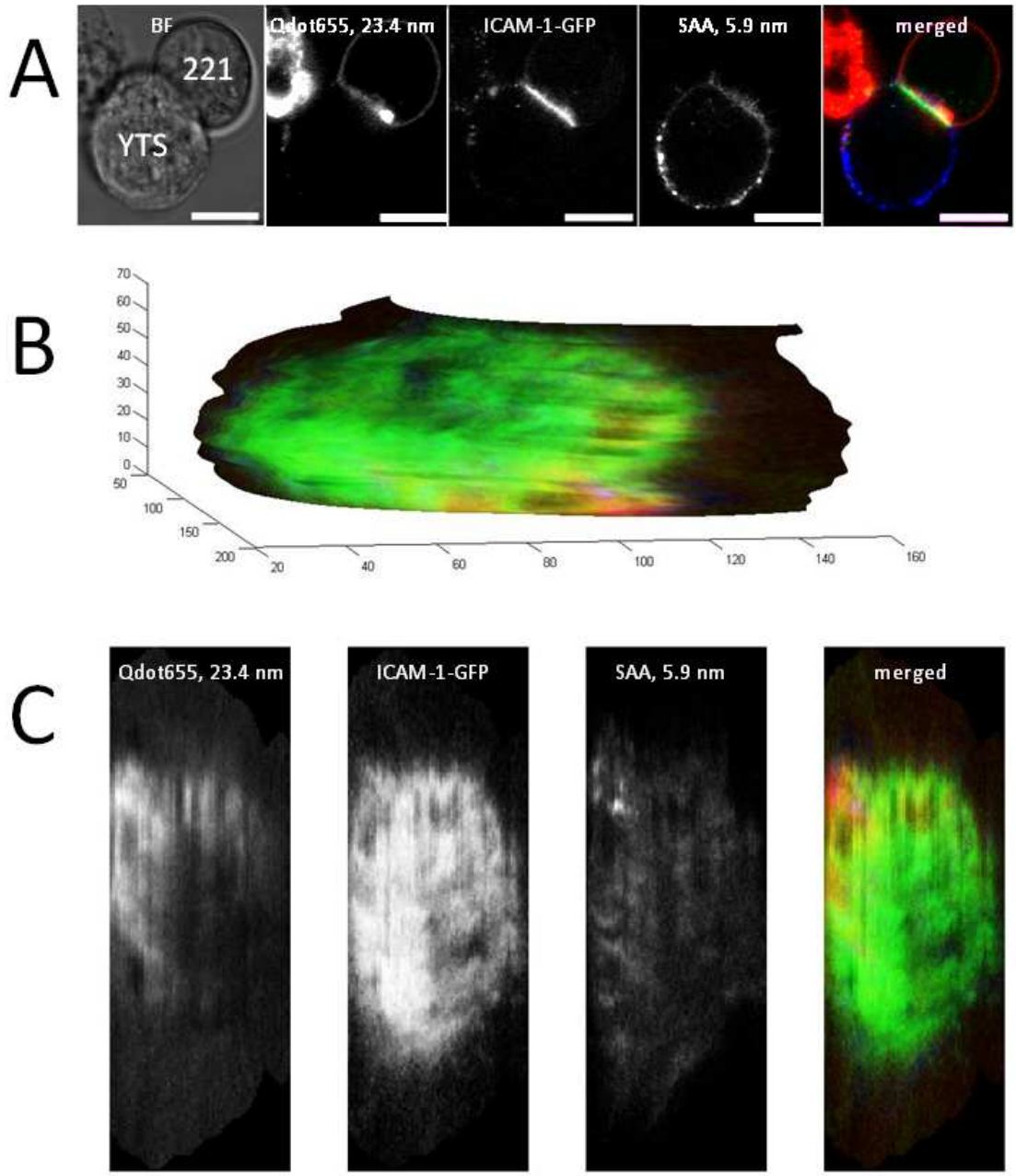


**Figure S7**. Synapse formed by 221/ICAM-1-GFP with YTS/KIR2DL1. In *(A)* a Z slice from a stack is shown; the images from left to right are the brightfield and red/Qdot655, green/ICAM-1-GFP, and blue/SA405 fluorescence channels of the merged image. In *(B)* the contact-surface reconstruction is shown. In *(C)* the 2D plot of the contact-surface is shown; the channels from left to right are in the same order as in *(A)*.

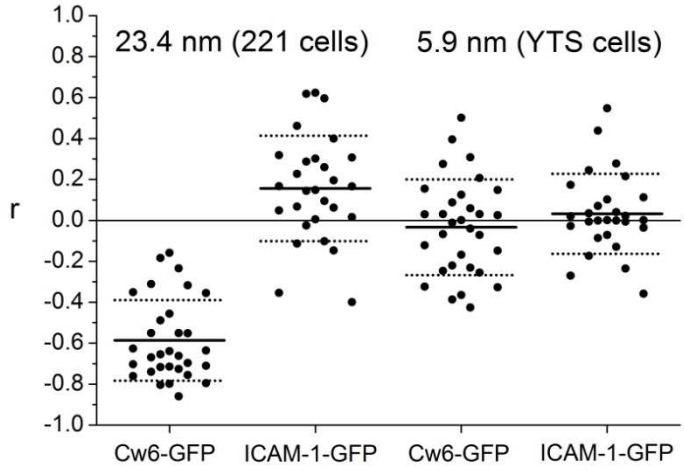


**Figure S8**. Intensity of the largest fluorescent particle does not show negative correlation to ICAM-1-GFP intensity. Intensity correlation coefficients in 221/Cw6-GFP-to-YTS/KIR2DL1 and 221/ICAM-1-GFP-to-YTS/KIR2DL1 cell-to-cell contacts are compared for Qdot655 (23.4 nm) (the two sets at the left) and SA (5.9 nm) (two sets at right).

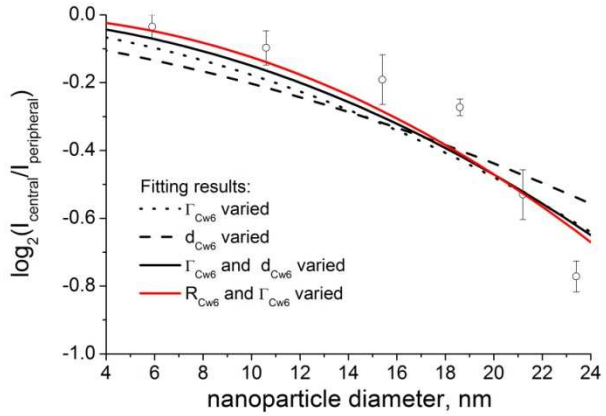


**Figure S9.** The central/peripheral fluorescent particle intensity ratios cannot be fitted by a lateral crowding-based model alone. The data has been fitted by varying different parameters in Eq. 1 (see text and Appendix S1). The open circles represent the combined data used in fitting. The dotted line represents best fit, when the surface number density of Cw6-GFP was varied ($\Gamma_{Cw6}$ = 385/μm$^2$ for the best fit, i.e. more than twice the actual estimate). The dashed line represents best fit for varying the diameter of Cw6-GFP ($d_{Cw6}$ = 12.1 nm for the best fit). The continuous line represent best fit for varying both $\Gamma_{Cw6}$ and $d_{Cw6}$ (subject to the constraints $d_{Cw6}\geq 3$ nm, $\Gamma_{Cw6}\geq 0$, resulting in $d_{Cw6}$ = 3 nm and $\Gamma_{Cw6}$ = 490/μm$^2$). The red continuous line indicates fit where Cw6-GFP central/peripheral ratio $R_{Cw6}$ and $\Gamma_{Cw6}$ were varied (resulting in $R_{Cw6}$=1.0001 and $\Gamma_{Cw6}$=31600/μm$^2$). Using all three parameters as adjustable ones makes the fitting very sensitive to initial values, but does not improve quality of the fits. Hence, even non-physical values of the parameters do not allow for a reasonable fit to data, using an equation based solely on lateral crowding, whereas the lateral crowding-based equation provides excellent agreement with data, without a single adjustable parameter up to the point where membrane bending-dependent exclusion is expected to become apparent (Fig. 5 *C*).

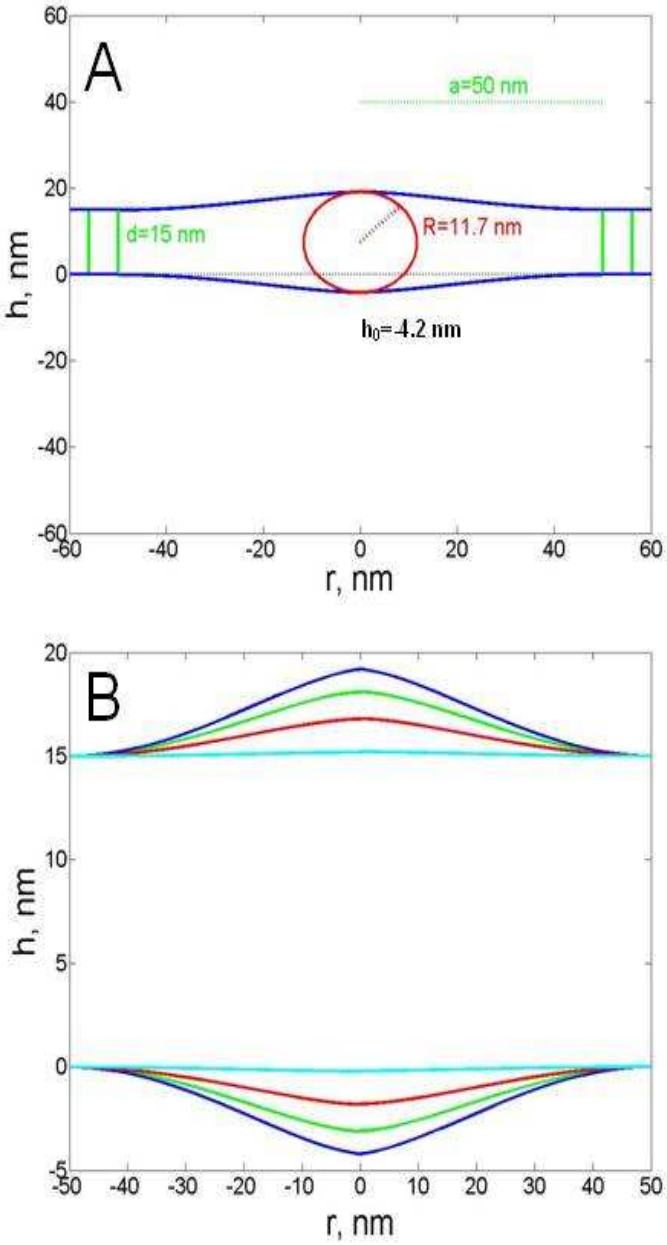


**Figure S10.** The evaluation of membrane bending free energy in a simple model. For the calculation of order of magnitude estimates we considered an axisymmetric system, where the HLA-Cw6-GFP/KIR2DL1 complexes (green vertical lines in *(A)*) force the membrane to flatness at radius r = a. The fluorescent particle at r = 0 (red outline in *(A)*) induces curvature to the membrane at r ≤ a if its radius R > 7.5 nm, i.e. more than half the membrane separation. When mirror symmetry in the vertical direction is assumed, the problem simplifies to solving the curvature in the lower membrane in *(A)*. The blue lines in *(A)* show the minimum free energy membrane profile for a=50 nm and R=11.7 nm. In *(B)* the minimum free energy profiles for a=50 nm and fluorescent particle diameters 15.4 nm (cyan line), 18.6 nm (red line), 21.2 nm (green line), and 23.4 nm (blue line).

**Appendix S1:** Derivation of Eq. 1

The scaled particle adsorption theory derives for the adsorption of particle A onto surface with arbitrary occupancy of particle B the adsorption level of particle A is (for concentrations of A far from saturating) (Eq. 13 in ref. (S1)):

$$\frac{\Phi_A}{\Phi_A^0} = (1-\Phi_B)\Lambda$$

(Eq. S1)

where $\Phi$ refers to fractional coverage of surface by the particle, the subscript defining particle type, while the superscript 0 refers to coverage in the absence of the other particle. $(1-\Phi_B)$ describes the available area, not accounting for packing defects, e.g. circular disks (of particle B) could never decrease $(1-\Phi_B)$ to zero as it is impossible to cover an area with circles completely, since there will always be area not covered at the contact of three closely packed circles. The entropy and packing contribution $\Lambda$ is defined as (S1):

$$\Lambda \equiv exp\left\{-f_R\Phi_B\left[2\epsilon f_c\frac{1}{1-\Phi_B}+f_a f_R\left(\frac{1-(\epsilon-1)\Phi_B}{(1-\Phi_B)^2}\right)\right]\right\}$$

(Eq. S2)

where $\epsilon$ is the shape factor for particle B (for a circle $\epsilon = 1$), $f_R$ is the ratio of characteristic dimensions (such as radii) of particles A and B, $f_c$ is the calculated as a ratio of two ratios, namely the circumference/characteristic dimension ratios (=2π for a circle) for particles A and B (for two circular disks $f_c$ = 1), and similarly $f_a$ is calculated as a ratio of two ratios, namely the particle area/(particle characteristic dimension)$^2$ (=π for a circular disks) for particles A and B (for two circular disks $f_a$ = 1). Here we approximate both the fluorescent particles and the receptor–ligand complexes as circular disks with given radii. Hence we obtain:

$$\Lambda \equiv exp\left\{-f_R\Phi_B\left[2\frac{1}{1-\Phi_B}+f_R\left(\frac{1}{(1-\Phi_B)^2}\right)\right]\right\}$$

(Eq. S3)

Given that the level of adsorption in the absence of B is only dependent on the reference state in solution, for adsorption of A onto surface of two different levels of B or likewise for distribution of particles A between two such domains on a surface we have from Eq. S1:

$$\frac{\Phi_{A1}}{(1-\Phi_{B1})\Lambda_1} = \frac{\Phi_{A2}}{(1-\Phi_{B2})\Lambda_2}$$

(Eq. S4)

Let us define $\rho \equiv \Phi_{B2}/\Phi_{B1}$ and $\Phi_B = \Phi_{B1}$, leading to the ratio of fractional surface coverage in domains 2 and 1 by particle A:

$$R = \frac{\Phi_{A2}}{\Phi_{A1}} = \frac{(1-\rho\Phi_B)exp\left\{-f_R\rho\Phi_B\left[2\frac{1}{1-\rho\Phi_B}+f_R\left(\frac{1}{(1-\rho\Phi_B)^2}\right)\right]\right\}}{(1-\Phi_B)exp\left\{-f_R\Phi_B\left[2\frac{1}{1-\Phi_B}+f_R\left(\frac{1}{(1-\Phi_B)^2}\right)\right]\right\}}$$

(Eq. S5)

For our purposes the ratio in Eq. S5 represents the predicted ratio of fluorescent particle surface concentration between regions 2 (central zone of the synapse) and 1 (peripheral zone of the synapse) with ρ representing the same ratio for Cw6-GFP, i.e. $\rho = R_{Cw6}$ (obtained from the fluorescence intensity levels), and $\Phi_B$ the fractional surface coverage by Cw6-GFP in the peripheral zone of the synapse. Since the ratios of radii and diameters are equal we replace $f_R$ with $f_D$ and obtain Eq. 1. Note that here we assume that the contribution of other proteins to differences in crowding in the central and peripheral zones of the synapse is so small that it can be ignored.

**Appendix S2:** Derivation of the curvature free energy for a symmetric double bump in a tension-free homogeneous bilayer

As discussed in the main text, the membrane curvature-mediated interactions are very complex and difficult to treat analytically. Hence, we merely wanted to estimate if the order of magnitude is correct by calculating the curvature free energy of a single double bump caused by a fluorescent particle in between the two bilayers. Even here, we will have to arbitrarily impose a condition defining the membrane outside the actual bump rather than evaluating the effect of receptor–ligand distribution outside the bump on the actual membrane curvature. We hence assume that the system is axisymmetric and that at the distance *a* from the center of the bump the membrane again becomes flat at the reference level (gradient=0), as imposed by the surrounding HLA-Cw6-to-KIR2DL1 complexes.

Because of the symmetry (see Fig. S10), we consider one bilayer in a Monge gauge that is valid as long as there are no overhangs. In a Monge gauge the level h describes the height of the bilayer locally below or above the reference plane and, as far the gradients are small, the free energy of the membrane in the absence of other forces and for zero spontaneous curvature is approximately

$$H \approx \frac{1}{2}\int dxdy[\kappa(\nabla^2 \mathrm{h})^2 + \sigma(\nabla \mathrm{h})^2]\,, \qquad \text{Eq. S6}$$

where κ is the membrane bending modulus and σ is the membrane tension. For the minimum energy solutions of this equation the first variation disappears and they satisfy the differential equation (S5)

$$\nabla^2(\nabla^2 - \lambda^{-2})\mathrm{h} = 0 \qquad \text{Eq. S7}$$

where λ is the ratio $\lambda := \sqrt{\frac{\kappa}{\sigma}}$, and for a tension-free membrane (σ = 0), the minimum energy solution may be found as a solution of the biharmonic equation

$$\nabla^4 \mathrm{h} = 0. \qquad \text{Eq. S8}$$

A very similar problem to ours has been treated by others (S5) who studied indentation caused by an AFM tip on a nanodrum pore. The solutions may be found as solutions of Eq. S7 if tension is to be included. When limited to an axisymmetric case, the general solution is (see ref. S5):

$$h(r) = h_1 + h_2 \ln\left(\frac{r}{\lambda}\right) + h_3 I_0\left(\frac{r}{\lambda}\right) + h_4 K_0\left(\frac{r}{\lambda}\right) \qquad \text{Eq. S9}$$

where values for $h_i$ are constants, and $I_0$ and $K_0$ are modified Bessel functions of the first and second kind. Similarly, for the tension-free case the axisymmetric solution is the axisymmetric solution of the biharmonic equation (Eq. S8) (S6)

$$h(r) = b_1 + b_2 \ln(r) + b_3 r^2 + b_4 r^2 \ln(r) \qquad \text{Eq. S10}$$

In our case, the region limited by the surrounding receptor–ligand complexes corresponds to radius of the nanodrum pore in ref. S5. The membrane must be continuous at the edges of the region as well as at the fluorescent particle/membrane contact. Hence from ref. S5 we obtain the boundary conditions

$h(a) = 0$ Eq. S11

$h'(a) = 0$ Eq. S12

where $h'$ = dh/dr, and *a* is the radius of the region limited by receptors.

We assume the fluorescent particle to be spherical and to have its center symmetrically with respect to the two membranes. When the membrane is in contact with fluorescent particle, the height

$$h(r) = -h_0 + R_{NP} - \sqrt{R_{NP}^2 - r^2},$$

where $h_0$ is the depth of indentation caused by the nanoparticle at r = 0 and hence at the contact point *c* of the membrane and the fluorescent particle

$$h(c) = -h_0 + R_{NP} - \sqrt{R_{NP}^2 - c^2}$$ Eq. S13

while the continuity of the membrane requires that the gradients (in an axisymmetric case the radial derivatives) are equal.

$$h'(c) = \frac{c}{\sqrt{R_{NP}^2 - c^2}}$$ Eq. S14

Hence, the solution can be found as the solution of Eq. S9 (if tension is included) or Eq. S10 (for the tension free case) that satisfies the boundary conditions in Eq. S11–S14. In our treatment we omit the membrane–fluorescent particle adhesion free energy. After the solution is found, the contact point $c$ is varied so as to give the minimum free energy solution. For ease of calculation we scale all the lengths in the system with the length $a$; i.e. set $a$=1 and present $h_0$, $R_{NP}$, and $r$ in proportion to $a$.

For the tension free case (Eq. S10), the boundary conditions then take the form

$$h(1) = b_1 + b_3 = 0$$
$$h'(1) = b_2 + 2b_3 + b_4 = 0$$
$$h(c) = b_1 + b_2 \ln(c) + b_3 c^2 + b_4 c^2 \ln(c) = -h_0 + R_{NP} - \sqrt{R_{NP}^2 - c^2}$$
$$h'(c) = b_2 \frac{1}{c} + b_3 c[2\ln(c) + 1] + 2b_4 c = \frac{c}{\sqrt{R_{NP}^2 - c^2}}$$

Eq. S14

The approximations made in our system will introduce a high level of uncertainty into our calculations, and we will in any case at best obtain order-of-magnitude estimates. In addition, the membrane tension $\sigma$ in biological membranes is typically very low, and hence we consider only the tension-free estimate. From the boundary conditions Eq. S14 we get the values for the constants for $c \neq 0$:

$$b_1 = -P \cdot (c^2 \ln c)$$
$$b_2 = -Q + P(c^2 - 1 - 2c^2 \ln c)$$
$$b_3 = P \cdot (c^2 \ln c)$$
$$b_4 = Q - P(c^2 - 1 - 2\ln c)$$

Eq. S15

where

$$Q = \frac{-h_0 + R_{NP} - \sqrt{R_{NP}^2 - c^2}}{(c^2 - 1)\ln c}$$

and

$$P = \frac{1}{4c^2(\ln c)^2 - c^4 + 2c^2 - 1}\left[\frac{c^2}{\sqrt{R_{NP}^2 - c^2}} - Q(2c^2 \ln c + c^2 - 1)\right]$$

Alternatively, if $c$=0,

$$b_1 = -h_0$$
$$b_2 = 0$$
$$b_3 = h_0$$
$$b_4 = -2h_0 .$$

Assuming constant bending modulus $\kappa$ as well as zero spontaneous curvature, because two symmetric bilayers are involved and the system is axially symmetric the curvature free energy is:

$$H \approx \kappa \int dr \int r d\theta (\nabla^2 \mathrm{h})^2 = 2\pi\kappa \left[\int_0^c dr\, r \left(\frac{1}{R_{NP}}\right)^2 + \int_c^1 dr\, r(4b_3 + 4b_4 + 4b_4 \ln r)^2\right] =$$
$$2\pi\kappa \left[\left(\frac{c}{R_{NP}}\right)^2 + 4(2b_3^2 + 2b_3 b_4 + b_4^2)(1 - c^2) - 8(2b_3 b_4 + b_4^2)c^2 \ln c - 8b_4^2 c^2 (\ln c)^2\right]$$

Eq. S16

By inserting the values of constants $b_3$ and $b_4$ (Eq. S15) in Eq. S16 one can find the value of $c$ that gives the minimum free energy. Due to complex dependence of $b_3$ and $b_4$ on $c$, the task of finding the zero of the derivative does not appear any simpler than finding $c$ that gives the minimum in $H$ in a straightforward numerical calculation. After the value of $c$ that gives the minimum free energy is known, the profiles can also be calculated. For the special case c=0 the free energy of the bump is simply given in terms of non-normalized original values (i.e. $h_0=(2R_{NP}-d)/2$ and $a$, too, has its original value rather than $a=1$) as

$$H=16\pi\kappa(h_0/a)^2 \qquad \text{Eq. S17}$$

that is a very good approximation if $h_0/a$ ratio is not very large (largest deviation from our numerical results was 0.7%;). Let us consider that the height difference would be accommodated by one bilayer alone, i.e. $h_0$ in Eq. S17 would be twice as large, but since there is only one bilayer, the final value must be divided by two. In other words, with this simple approximation, the free energy for accommodating a protein with a larger extracellular domain than preferred intermembrane spacing is twice as large when only one of the membranes can bend. Hence solid-supported lipid bilayer-based artificial immune synapses should be much more sensitive to height differences; assuming $a$ = 50 nm, height difference of 6 nm ($h_0$=3 nm in Eq. S17) and $\kappa=0.3\times10^{-19}$ J, the expected central/peripheral ratios based on this simple approximation would be 0.28 in the "cell–cell" and 0.08 in the "SLB–cell" systems. Note that these values should not be considered as predictions, as they do not take in to account the real complexity of the situation, but they demonstrate the effect that using SLBs is expected to have.

Very different values of $\kappa$ for different membranes have been reported, and the value of $\kappa$ is sensitive to the cholesterol content of the membrane, reaching values up to $3\times10^{-19}$ J for fluid membranes containing tens of mol% cholesterol (S7). In the absence of cholesterol, the values of $\kappa$ reported for fluid membranes are mostly in the region 0.1–1 $\times10^{-19}$ J (S7). At our experimental temperature of ~310 K $k_BT\approx4.28\times10^{-21}$ J. We calculated the membrane curvature free energies for three different values of $\kappa$, $0.1\times10^{-19}$ J, $0.3\times10^{-19}$ J, and $1.0\times10^{-19}$ J, as well as for five different radii of the region: 50, 100, 150, 200, and 250 nm. The lower limit for the radius of the region was set as 50 nm, as it seems unlikely that a region much smaller than this would be realistic, for the calculated mean distance between HLA-Cw6-GFP molecules in the central region of synapse is approx. 45 nm. The upper limit of the radius was set at 250 nm, as regions devoid of HLA-Cw6-GFP larger than 500 nm in diameter should be visible given the resolution of the microscope. To make the comparison to the data more clear, we present the data as the expected fluorescent particle central/peripheral ratio based on partitioning depending solely on membrane curvature free energy according to the Boltzmann distribution. The values show that particularly in the mid-range of $\kappa$ estimates the membrane bending elasticity-driven expulsion of the fluorescent particles agrees reasonably well with the experimental results. Note that (in addition to the real complexity of protein–particle, particle–particle, and protein–protein interactions) we have neglected several factors that may affect the free energy cost of inserting the fluorescent particle between the membranes. First, the clustering of fluorescent particles is expected to decrease the bending free energy cost/particle. This clustering will be driven by the resulting decrease in bending free energy. Second, it is possible that the membrane may adhere onto the fluorescent particle surface. This is expected to decrease the free energy cost. Third, we neglected the small membrane tension observed in cell membranes. This tension will increase the free energy cost of creating a bump. Fourth, we did not consider the locally varying spontaneous bilayer curvature that could decrease or increase the free energy cost of creating the bump. Fifth, the lateral dimension of the curvature defect ("$a$" in our simple model) is expected to different for each particle size, depending on protein distribution-related entropy considerations and packing in the central zone of the synapse. In addition, of course, the

actual values of membrane tension, bending modulus, and spontaneous curvature in the immune synapse are unknown. Combined with realistic simulations and super-resolution imaging (S8) (to observe clustering), our method could allow for the deduction of these very values.

**Table S1**. The characteristics of cells (N=12) analyzed for quantification of the HLA-Cw6-GFP numbers in the synapse.

| **Property** | **Value** |
|---|---|
| mean volume | 3420±370 $\mu m^3$ |
| mean area | 1930±320 $\mu m^2$ |
| mean of area/(area of sphere of equal volume) | 1.68±0.15 |
| mean total GFP intensity | 2.0±0.3 $\times 10^7$ a.u. |
| mean fraction of GFP in membrane | 0.69±0.03 |
| mean fraction of NP in membrane | 0.83±0.01 |
| mean GFP surface number density in membrane[1] | 134±20 molecules/$\mu m^2$ |
| mean GFP surface number density in the peripheral zone of synapse | 212±32 molecules/$\mu m^2$ |

[1]Calculated from the flow cytometry analysis of mean number of GFP molecules/cell surface = 250 000 and the total cell and membrane GFP intensities.

**Table S2**. Predicted fluorescent particle central/peripheral ratio based on the membrane curvature free energy of a bump, with $\kappa = 0.1 \times 10^{-19}$ J

| | **particle diameter** | | | |
|---|---|---|---|---|
| **region radius** | 15.4 nm | 18.6 nm | 21.2 nm | 23.4 nm |
| 50 nm | 0.998 | 0.859 | 0.637 | 0.439 |
| 100 nm | 1.000 | 0.963 | 0.893 | 0.813 |
| 150 nm | 1.000 | 0.983 | 0.951 | 0.912 |
| 200 nm | 1.000 | 0.991 | 0.972 | 0.950 |
| 250 nm | 1.000 | 0.994 | 0.982 | 0.967 |
| experimental | 0.876 (0.833–0.921) | 0.828 (0.814–0.842) | 0.693 (0.658–0.729) | 0.586 (0.568–0.605) |
| experimental / scaled particle prediction | 0.987 (0.939–1.039) | 0.971 (0.954–0.987) | 0.842 (0.800–0.886) | 0.736 (0.713–0.760) |

**Table S3**. Predicted fluorescent particle central/peripheral ratio based on the membrane curvature free energy of a bump, with $\kappa = 0.3\times10^{-19}$ J

| | **particle diameter** | | | |
|---|---|---|---|---|
| **region radius** | 15.4 nm | 18.6 nm | 21.2 nm | 23.4 nm |
| 50 nm | 0.994 | 0.633 | 0.258 | 0.085 |
| 100 nm | 0.999 | 0.892 | 0.713 | 0.537 |
| 150 nm | 0.999 | 0.951 | 0.860 | 0.759 |
| 200 nm | 1.000 | 0.972 | 0.919 | 0.856 |
| 250 nm | 1.000 | 0.982 | 0.947 | 0.905 |
| experimental | 0.876 (0.833–0.921) | 0.828 (0.814–0.842) | 0.693 (0.658–0.729) | 0.586 (0.568–0.605) |
| experimental / scaled particle prediction | 0.987 (0.939–1.039) | 0.971 (0.954–0.987) | 0.842 (0.800–0.886) | 0.736 (0.713–0.760) |

**Table S4**. Predicted fluorescent particle central/peripheral ratio based on the membrane curvature free energy of a bump, with $\kappa = 1.0\times10^{-19}$ J

| | **particle diameter** | | | |
|---|---|---|---|---|
| **region radius** | 15.4 nm | 18.6 nm | 21.2 nm | 23.4 nm |
| 50 nm[1] | 0.981 | 0.218 | 0.011 | 0.000 |
| 100 nm | 0.995 | 0.684 | 0.323 | 0.126 |
| 150 nm | 0.998 | 0.844 | 0.606 | 0.398 |
| 200 nm | 0.999 | 0.909 | 0.754 | 0.596 |
| 250 nm | 0.999 | 0.941 | 0.835 | 0.718 |
| experimental | 0.876 (0.833–0.921) | 0.828 (0.814–0.842) | 0.693 (0.658–0.729) | 0.586 (0.568–0.605) |
| experimental / scaled particle prediction | 0.987 (0.939–1.039) | 0.971 (0.954–0.987) | 0.842 (0.800–0.886) | 0.736 (0.713–0.760) |

**Supporting Material References**

S1. Chatelier, R. C., and A. P. Minton. 1996. Adsorption of globular proteins on locally planar surfaces: models for the effect of excluded surface area and aggregation of adsorbed protein on adsorption equilibria. *Biophys. J.* 71:2367–2374.
S2. Li, C., C.-Y Kao, J. C. Gore, and Z. Ding. 2008. Minimization of region-scalable fitting energy for image segmentation. *IEEE Transact. Image Process.* 17:1940–1949.
S3. Garcia, D. 2010. Robust smoothing of gridded data in one and higher dimensions with missing values. *Comput. Stat. Data Anal.* 54:1167–1178
S4. Rajan, J., K. Kannan, and M. R. Kaimal. 2008. An improved hybrid model for molecular image denoising. *J. Math. Imaging. Vis.* 31:73–79.
S5. Norouzi, D., M. M. Müller, and M. Deserno. 2006. How to determine local elastic properties of lipid bilayer membranes from atomic-force-microscope measurements: a theoretical analysis. *Phys. Rev. E* 74: 061914-1–061914-12.
S6. Timoshenko, S. P. and J. N. Goodier. 1970. Theory of Elasticity, 3rd ed. McGraw-Hill Book Co. Singapore.
S7. Marsh, D. 2006. Elastic curvature constants of lipid monolayers and bilayers. *Chem. Phys. Lipids* 144: 146–159.
S8. Hell, S. W. 2007. Far-field optical nanoscopy. *Science* 316: 1153–1158.